Modeling of Electric Vehicles Dynamics with Multi-Bond Graphs

Luis I. Silva, Guillermo A. Magallan, Pablo M. de la Barrera, Cristian H. De Angelo and Guillermo O. García
Grupo de Electrónica Aplicada, Facultad de Ingeniería, Universidad Nacional de Río Cuarto,
Ruta Nac. #36 Km. 601, X5804BYA Río Cuarto, Córdoba, Argentina. lsilva@ing.unrc.edu.ar

***Abstract*—The construction of a model that represents the behavior of an Electric Vehicle is studied in detail. The contribution of this work is twofold. On one hand an efficient and compact way to model dynamical systems is introduced. On the other hand, the power interchange between the electrical and mechanical sub-models allows a deep understanding of the dynamics involved in electrically driven vehicles. The approach used to model the mechanical parts (chassis, suspension, wheels) and the induction motors is the Multi-Bond Graph based in models discussed in recent literature. Then these models are integrated in order to form the complete model that simulates the whole system dynamics. Simulation results are aimed to illustrate the electromechanical interaction (ABS, regenerative braking, etc) as well as the evolution of certain variables during a risky situation. Conclusions are obtained based on these results.**

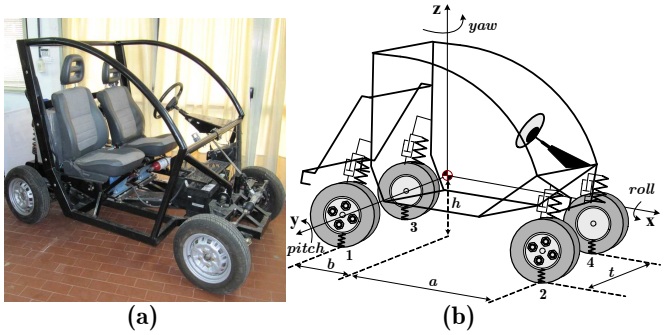

Fig. 1. a) Vehicle prototype. b) Vehicle geometry

I. Introduction

Nowadays there is an enormous pressure to improve fuel economy and reduce vehicle emissions. As a result, alternative transportation solutions have been investigated in the last decades. The proposed vehicle is supposed to fulfill many conditions such as: been affordable and profitable. They are also supposed to use the whole structure that standard vehicles have utilized until now as much as possible. Electric Vehicles (EV) and/or Hybrid Electric Vehicles (HEV) have been studied as a possible solution to meet these goals.

This work addresses the modeling and simulation of an EV. A model capable to reproduce the whole dynamics of the mechanical components is firstly presented. Secondly it is developed a model for the traction mechanism that can adopt different configurations [1], depending on its location and the type of motors used. It is composed by two independently controlled induction motors (IM) located in the rear wheels. Once the models of the IM are developed, they are coupled to the rear wheels (models) to obtain the complete model. This model does not contemplate dynamics involved from energy source up to the IMs. This feature makes the model applicable to EV´s but also to series HEV´s where the propulsion is always obtained from the electric motors.

The modeling and simulation of vehicle dynamical behavior is carried out using the Multi-Bond Graph (MBG) approach [2][3][4]. A brief introduction to this approach is included in the Appendix. It is adequate to model large scale physical systems independently of their nature. So, it becomes a powerful tool when the interaction of complex sub-systems with different nature needs to be evaluated. It consists in the utilization of the Multi-Bond to represent the power flow between different components. In the same way each subsystem can interact with others through its input/output Multi-Bonds and the hierarchical modeling becomes straightforward.

To create the models Dymola [5] is used. It is an integrated environment for developing models in Modelica language. An original contribution of this work lies in the utilization of the library for MGB´s and its applications in 3-D mechanics [6]. Methods based on deriving the set of differential equations that govern the element dynamical behavior are time consuming and error prone. Conversely, with the graphical programming it is no necessary to introduce explicitly these equations making the modeling task faster and in a modular way.

The model in Dymola environment allows to visualize and study in depth the interaction between mechanical and electrical sub-models. It helps in the design stage and allows the evaluation of the prototype response under faulty or dangerous conditions even prior to the actual construction.

Section II is devoted to describe and model the mechanical components involved in the vehicle. In Section III the electric motor is modeled. Along Section IV mechanical and electric sub-models are connected to achieve the complete model. Section V shows simulation results of the complete system performance. Conclusions are discussed in Section VI.

II. Mechanical Characteristics and Modeling

The model is in correspondence with the prototype under construction by the Applied Electronic Group and the Department of Mechanics at the National University of Rio Cuarto (see Fig. 1.a). The geometry is seen in Fig. 1.b and responds to the so-called neighborhood electric vehicle. The physical principles and modeling is discussed in detail in [7].

978-1-4244-8218-4/10/$26.00 ©2010 IEEE

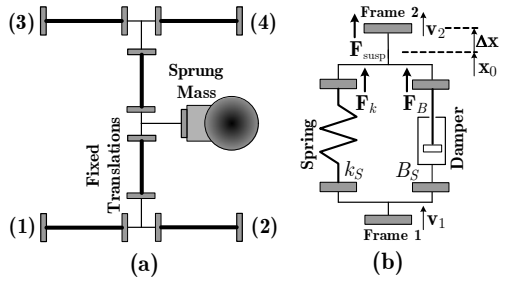

Fig. 2. a) Chassis Model b) Suspension model

A. Chassis

The model of the chassis, as represented in Fig. 2.a is composed by a sprung mass and a set of fixed translations. For the translational dynamics the sprung mass behaves like a lumped mass but for the rotational dynamics it contains the inertia tensor thus acting like a rigid body. The laws for the 3-D body motion are given by the Euler's equations

$$\mathbf{F} = m\,\mathbf{a} \tag{1}$$

$$\mathbf{T} = \left(\frac{d\mathbf{L}}{dt}\right)_{\text{local}} + \boldsymbol{\omega}\times\mathbf{L} \tag{2}$$

where $\mathbf{F} = [F_x\ F_y\ F_z]$ and $\mathbf{T} = [T_x\ T_y\ T_z]$ are the forces (in the global frame) and torques (in the local frame) applied over the rigid body, respectively. $\mathbf{L}$ and $\boldsymbol{\omega}$ represent the angular momentum and angular velocity.

The internal structure of fixed translations in MBG is explained in the Example of Appendix. These fixed translations are used to compose the undeformable structure of the chassis that projects the efforts and flows from the sprung mass - located in the center of gravity- toward the points where the suspensions are mechanically connected in the frames noted with 1, 2, 3 and 4.

B. Suspension

The suspension system is composed by four suspensions that couple each of the wheels to the chassis. Each suspension contains an ideal spring and a damper. Fig. 2-b shows the spring-damper connection that corresponds to the real mechanical configuration.

The total suspension force ($\mathbf{F}_{\text{susp}}$), the spring force ($\mathbf{F}_B$) and the damper force ($\mathbf{F}_{\text{susp}}$) are given by

$$\mathbf{F}_{\text{susp}} = \mathbf{F}_B + \mathbf{F}_k;\ \mathbf{F}_B = B_S\left(\mathbf{v}_2 - \mathbf{v}_1\right); \mathbf{F}_k = -k_S\boldsymbol{\Delta}\mathbf{x} \tag{3}$$

where velocities on frames 1 and 2 are $\mathbf{v}_1$ and $\mathbf{v}_2$. $\boldsymbol{\Delta}\mathbf{x}$ is the displacement respect to the rest position ($\mathbf{x}_0$).

C. Wheel and Tyres

The dynamic behavior of the wheels is represented in two different BG models coupled by signals (see Fig. 3-a). One part is devoted to the translational dynamics. It includes the calculation of the normal force at the contact patch (F_N) based on the vertical dynamics. The longitudinal/lateral forces (F_x/F_y) depend on the tyre characteristics and are of crucial importance for the dynamic behavior of the vehicle. These forces are evaluated in the "Pacejka" block using experimental curves [8]. The rotational dynamics receives the torque generated by the IM (T_e) and calculates its angular velocity (ω_r). The torque balance also includes: rolling resistance, inertia momentum of the wheel (I_W) and the opposition torque due to the longitudinal force on the patch contact at distance r_W. The wheel model was wrapped (Fig. 3-b) and provided with a frame to connect with the suspension, a single bond to interact with the IM and receives the steering (δ).

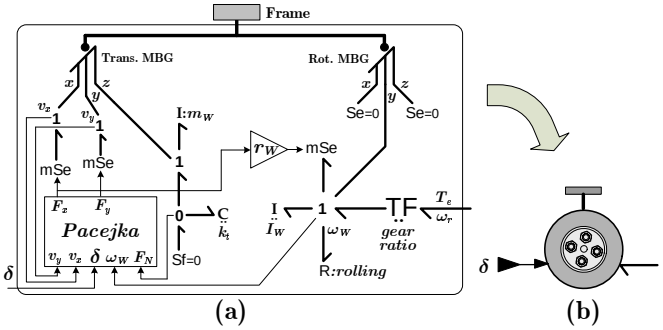

Fig. 3. a) BG model of the wheel. b) External representation in Dymola.

Eq. (4) shows that the longitudinal force ($\mathbf{F}_{\text{long}}$) is proportional to F_N and to the adherence coefficient μ_x. In the adopted model, μ_x depends only on the longitudinal slip (σ) that is given by (5).

$$\mathbf{F}_{\text{long}} = \mu_x\ \mathbf{F}_N \tag{4}$$

$$\sigma = \frac{(\omega_W.r_W - V_X)}{\max\{V_X, \omega_W.r_W\}} \tag{5}$$

where V_X is the longitudinal speed of the vehicle. ω_W and r_W are the wheel angular speed and radius respectively.

The dependence of μ_x respect to (σ) is shown in Fig. 4. A remarkable characteristic is that for $\sigma \geq 0.09$ F_{long} decays. This phenomenon can be seen both during a sudden acceleration and deceleration.

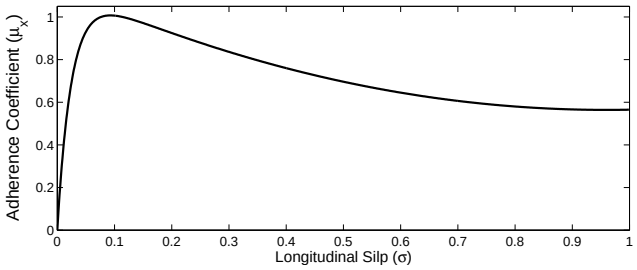

Fig. 4. Adherence Coefficient vs. Longitudinal Slip.

III. Electrical Features and Model

The prototype has dual-motor configuration in which two electric motors separately drive the rear wheels via fixed

gearing. Both motors are identical and their parameters are presented in Table I.

TABLE I
TRACTION MOTOR SPECIFICATIONS

Power	3 kW 4 hp
Rated line voltage	28 V_{rms}
Rated current	81.56 A_{rms}
Pairs of poles	2
Speed	1455 r/min
r_s	10.476 mΩ
r'_r	22.231 mΩ
L_m	1.21 mH
L_{ls}	89.03 μH
L'_{lr}	89.03 μH

The set of equations concerning voltage and flux linkage in q-d coordinates [9] are presented bellow

$$\mathbf{v}_{qds} = \mathbf{R}_s \mathbf{i}_{qds} + \omega \mathbf{J} \boldsymbol{\lambda}_{qds} + \dot{\boldsymbol{\lambda}}_{qds} \quad (6)$$

$$\mathbf{v}'_{qdr} = \mathbf{R}_r \mathbf{i}'_{qdr} + (\omega - \omega_r)\, \mathbf{J} \boldsymbol{\lambda}'_{qdr} + \dot{\boldsymbol{\lambda}}'_{qdr} \quad (7)$$

$$\boldsymbol{\lambda}_{qds} = \mathbf{L}_s \mathbf{i}_{qds} + \mathbf{L}_m \mathbf{i}'_{qdr} \quad (8)$$

$$\boldsymbol{\lambda}'_{qdr} = \mathbf{L}_r \mathbf{i}'_{qdr} + \mathbf{L}_m \mathbf{i}_{qds} \quad (9)$$

where

$$\mathbf{v}_{qds} = \begin{bmatrix} v_{qs} & v_{ds} \end{bmatrix}^T \;;\; \mathbf{v}'_{qdr} = \begin{bmatrix} v'_{qr} & v'_{dr} \end{bmatrix}^T \quad (10)$$

$$\mathbf{i}_{qds} = \begin{bmatrix} i_{qs} & i_{ds} \end{bmatrix}^T \;;\; \mathbf{i}'_{qdr} = \begin{bmatrix} i'_{qr} & i'_{dr} \end{bmatrix}^T \quad (11)$$

$$\boldsymbol{\lambda}_{qds} = \begin{bmatrix} \lambda_{qs} & \lambda_{ds} \end{bmatrix}^T \;;\; \boldsymbol{\lambda}'_{qdr} = \begin{bmatrix} \lambda'_{qr} & \lambda'_{dr} \end{bmatrix}^T \quad (12)$$

$$\mathbf{R}_s = R_s \mathbf{I}_{2x2} \;;\; \mathbf{R}'_r = R'_r \mathbf{I}_{2x2} \quad (13)$$

$$\mathbf{L}_s = (L_{ls} + L_m)\, \mathbf{I}_{2x2} \;;\; \mathbf{L}'_r = (L'_{lr} + L_m)\, \mathbf{I}_{2x2} \quad (14)$$

$$\mathbf{L}_m = L_m \mathbf{I}_{2x2} \;;\; \mathbf{J} = \begin{bmatrix} 0 & 1 \\ -1 & 0 \end{bmatrix} \quad (15)$$

all variables are referred to an arbitrary reference frame rotating with angular velocity $\omega = d\rho/dt$. Angle ρ is the d-axis position. $\mathbf{I}_{2x2}$ is the 2 by 2 identity matrix.

Electromagnetic torque as function of electrical variables is given by

$$T_e = k\ P\ L_m \left(i_{qs} i'_{dr} - i_{ds} i'_{qr}\right) \quad (16)$$

where k is a constant that depends on the chosen transformation (k=1 for power invariant) and P represents the pairs of poles in the IM. The above equations suggest the equivalent circuit shown in Fig. 5.

Here it is difficult to see the power conservation between electrical and mechanical variables. Therefore, for relating both domains and making this conservation clear, modulated gyrators (**MGY**) were used, see Fig. 6. From figure the following equation can be derived

$$e'_{qr} = P\ \lambda'_{dr} \omega_r \;;\; e'_{dr} = P\ \lambda'_{qr} \omega_r \quad (17)$$

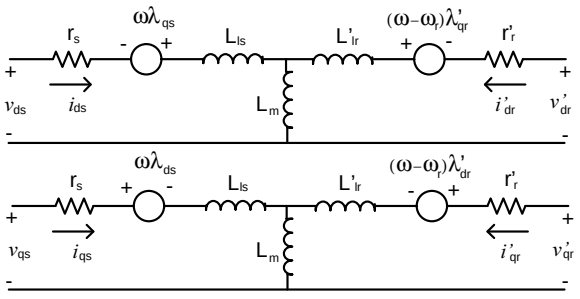

Fig. 5. Equivalent circuit in q-d frame.

taking into account that the **MGY**'s do not add or dissipate power and using the power conservation in the "**1**" the following equation can be obtained

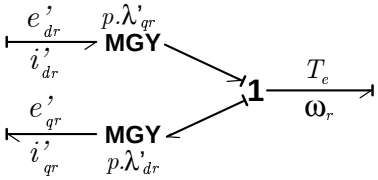

Fig. 6. Structure that relates electrical domain with mechanical domain.

$$T_e \omega_r = e'_{dr} i'_{dr} - e'_{qr} i'_{qr} \quad (18)$$

From (17) and (18) an alternative expresion for T_e is presented (can be deduceded from (9) and (16) for k=1):

$$T_e = P \left(\lambda'_{qr} i'_{dr} - \lambda'_{dr} i'_{qr}\right)$$

In order to keep consistency with the mechanical model, both circuits of the IM equivalent circuit of Fig. 5 can be represented in a MBG of cardinality two. The resulting model [11] is presented in an compact diagram shown in Fig. 7.

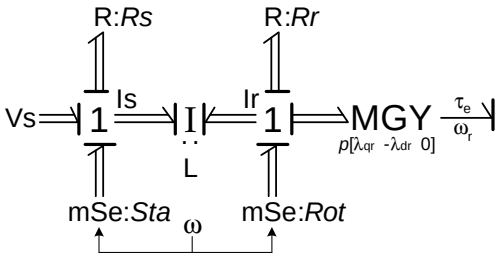

Fig. 7. IM representation with MBG.

The variables indicated in Fig. 7 are

$$\begin{aligned} \mathbf{Sta} &= \begin{bmatrix} \omega\lambda_{qs} & -\omega\lambda_{ds} \end{bmatrix}^T \\ \mathbf{Rot} &= \begin{bmatrix} \omega\lambda'_{qr} & -\omega\lambda'_{dr} \end{bmatrix}^T \end{aligned} \quad (19)$$

$$\mathbf{L} = \begin{bmatrix} \mathbf{L}_s & \mathbf{L}_m \\ \mathbf{L}_m & \mathbf{L}_r \end{bmatrix} \quad (20)$$

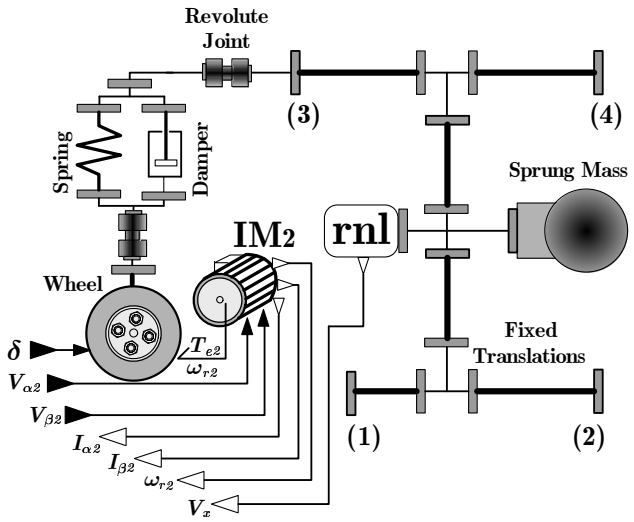

Fig. 8. Complete connection of Wheel and Suspension in Dymola.

Torque control and speed control were implemented using a Direct Field Oriented Control (DFOC) [12]. The fundamental idea is to work with IM model in q-d coordinates aligned with the rotor flux. This model allows independent control of rotor flux and motor torque.

For torque control, the reference torque is the same for both wheels and is given by the accelerator (or brake) pedal.

In speed control mode, an outer speed control loop is added. Now, the accelerator (or brake) pedal provides the speed reference. The error of this external controller commands the torque control loop previously commented. Details of the implementation are considered beyond the scope of this work.

IV. Complete Model

For a complete model to be obtained, all the sub-systems previously analyzed must be interconnected. The assembling is carried out in the same way the physical interaction occurs i.e. for rigid connections the frames are directly coupled otherwise a joint that allows certain degrees of freedom (relative movements) is interposed. The connection between the suspension system and the chassis is carried out through a revolute joint (it permits relative rotation along one axis), which allows the chassis pitch movement while each suspension remains in vertical position. Similarly the lower end of the suspension system connects to the wheel's frame via a revolute joint. This connection allows the spinning of the wheel. Fig. 8 shows the complete connection of the left rear wheel and suspension. The connections of the other three wheels are similar except that front wheels do not have traction motors. The incorporation of a non-lineal resistance "**rnl**" that models the dragging force only along longitudinal direction can also be observed in the same figure. The inputs of this sub-system are the steering angle (δ), which is always zero for rear wheels and the reference voltages applied to the IM. Currents and rotor angular speed are the outputs necessary to implement both DFOCs.

V. Simulation Results

The mechanical model was validated using the parameters of a Renault Clio RL 1.1. and comparing with [13]. After that, the parameters loaded in the mechanical model were in correspondence with the prototype built (shown in Table II) and several maneuvers were simulated in order to check consistency in the dynamical behavior. In the following subsections three different situations are studied.

TABLE II
Vehicle parameters

Aerodynamics coefficient (C_{drag})	0.5
Frontal area (A_f)	1.4 m^2
Air density (ρ)	1.225 $\frac{\mathrm{kg}}{\mathrm{m}^3}$
Vehicle mass (m)	960 kg
Tyres, type and dimensions	$14570R13S$
Tread distance (t)	1.10 m
Distance from CG to front axes (a)	1.02 m
Distance from CG to rear axes (b)	0.68 m
Pneumatic tyre radius (unloaded) (r_w)	0.268 m
Unsprung masses (at each wheel) (m_w)	38.42 kg
Tyre vertical stiffness	150000 $\frac{\mathrm{N}}{\mathrm{m}}$
Tyre inertia (I_w)	1.95 kgm^2
Damper coefficient (B_s)	483 $\frac{\mathrm{Ns}}{\mathrm{m}}$
Suspension stiffness (k_s)	23600 $\frac{\mathrm{N}}{\mathrm{m}}$
Yaw Inertia (I_{yy})	352 kgm^2
Pitch Inertia (I_{zz})	356 kgm^2
Roll Inertia (I_{xx})	152 kgm^2

A. Brake maneuver (with/without ABS)

The vehicle is driven straight with equal torque on both rear wheels. As result it travels with constant speed of $51\ \mathrm{km/h}$. At $t = 2.15\ \mathrm{s}$ a sudden brake is applied. For the first case it is a reverse torque that blocks both rear wheels. For the second case the control of the IMs is switched to speed control to produce the ABS that is implemented by controlling the wheels speed in order to keep $\delta = 0.09$ where the maximum brake force is generated (see Fig. 4). The different longitudinal forces on the patch contact after $2.15\ \mathrm{s}$ is seen in Fig. 9 where the force without ABS is considerably smaller than the ABS case. Fig. 10-a shows the velocities of the CG (noted as Vx) and tangential to the wheel. The blockage becomes evident immediately after the brake is applied. The time needed to stop is $5.35\ \mathrm{s}$ and continued a distance of $38\ \mathrm{m}$. For the second case (Fig. 10-b) the ABS leads the vehicle to rest faster ($3.25\ \mathrm{s}$) and within a shorter brake distance ($23\ \mathrm{m}$).

B. Brake maneuver (Blockage)

The electromechanical power transference changes from one case to the other. The blockage restricts the possibility of regenerative braking and the mechanical power is zero after the blockage is produced. Electrical power takes positive sign flowing from the source and being dissipated in the windings of the IM (here the motor has high current and torque). When the energy (in Fig. 11 is taken as positive from the IM toward the wheel) is analyzed, it becomes clear that ABS helps to recover the cinematic energy. In the first case it is delivered $\approx$9 kJ. Conversely with ABS $\approx$25 kJ were recovered.

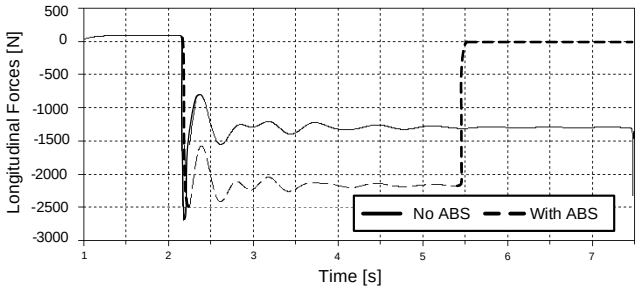

Fig. 9. Longitudinal forces with/without ABS.

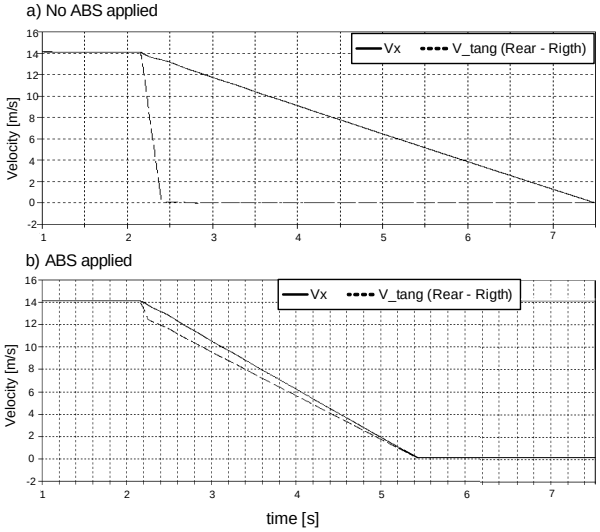

Fig. 10. Velocities of CG and tangential to wheel with/without ABS.

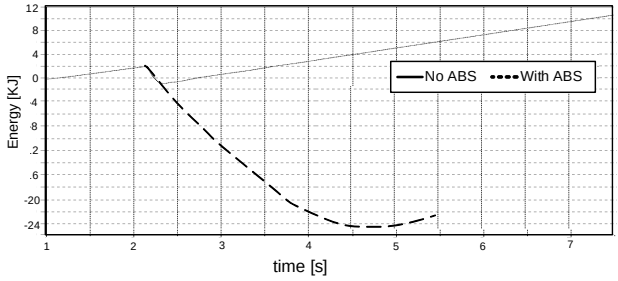

Fig. 11. Energy recovered by regenerative braking with/without ABS.

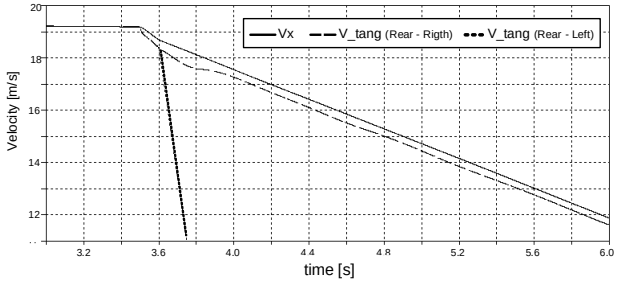

Fig. 12. Velocities of CG and tangential to wheel blocked and non-blocked.

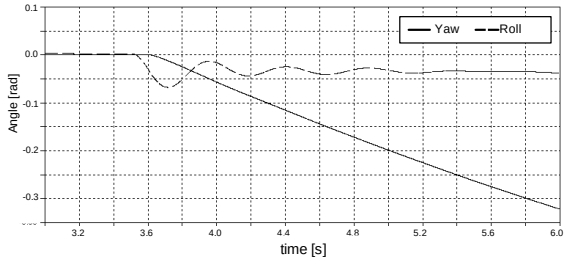

Fig. 13. Yaw and Roll evolution during blockage.

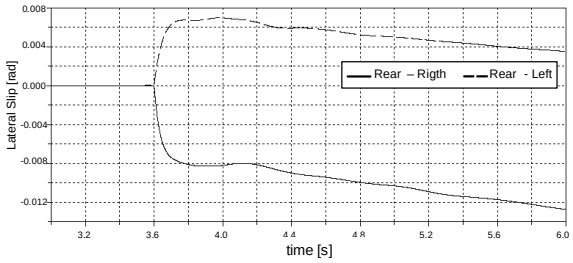

Fig. 14. Lateral slip of rear and frontal wheels during blockage.

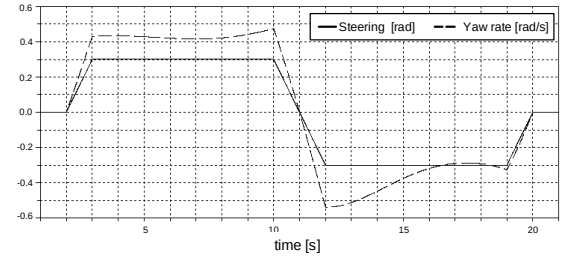

Fig. 15. Steering applied and Yaw rate during zigzag.

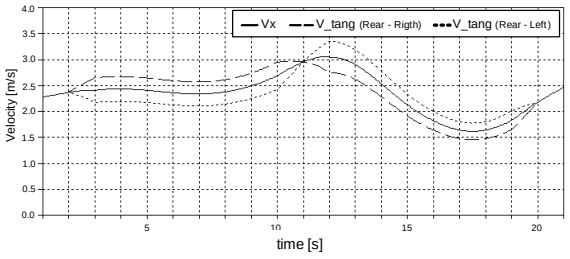

Fig. 16. Velocities of CG and tangential to rear wheels during zigzag.

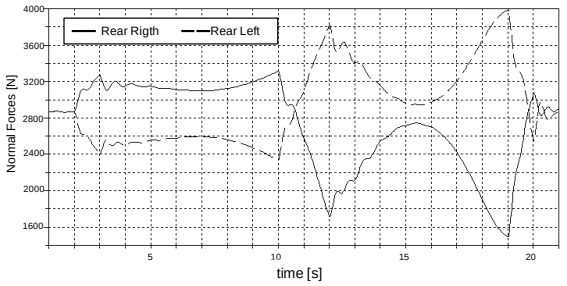

Fig. 17. Normal forces on the patch contact of rear wheels during zigzag.

The second experiment shows a situation where both left wheels are blocked during brake. The vehicle is driven at a constant speed of $70\ \mathrm{km/h}$ and after 3.5 seconds the brake is applied (mechanical brake on frontal wheels). In 0.1 s later ($t = 3.6$ s) left wheels are blocked and right wheels keep braking along. The vehicle continues to slow down as shown in Fig. 12 but the tangential velocities of the blocked and non-blocked wheels are absolutely different.

An important yaw angle appears (Fig. 13) due to the asymmetry on the longitudinal forces. This yaw rate produces load transference toward the left side and negative roll angle occurs. Finally, the lateral slip can be seen in Fig. 14.

C. Steering response (zigzag maneuver)

The last experiment consists of a large zigzag maneuver that starts with a violent turn toward left and then rigth.

It is applied the same constant torque on each rear wheel emulating the traditional mechanical differential [14]. This path trajectory results from the steering in Fig. 15. This figure also shows the yaw rate of the vehicle. At $t = 11$ s the vehicle changes the turning direction from left to right. Fig. 16 shows that before this inflexion point the left wheel moves slower (is the inner wheel) and after that it moves faster (is the outer).

Despite the low speed, load transference toward outer wheels is significant. This phenomenon is seen in Fig. 17.

VI. Conclusion

In this work the Multi-Bond Graph based model of the mechanical and electrical components of an EV and/or HEV is presented. The models construction was performed in a modular way. A clear benefit is the compactness and resemblance with a real vehicle assembling.

By simulation, it was proved that even with normal maneuvers the stability of the vehicle is in risk. It was also possible to visualize the power interaction between the mechanical and electrical parts during a sudden brake. The versatility of the model permits to simulate many other situations and helps to understand the dynamics of electrically driven vehicles.

Further work will be oriented to validate the proposed model using experimental results from the prototype in a first stage. The second stage will be focused on the hybridization of the prototype. To that purpose, the combustion engine will be modeled and a supervisor strategy will be included. This larger model extends the application to all the HEV´s configurations.

Appendix

Fundamentals of Multi-Bond Graph (MBG)

The brief description of this approach is based on [15]. MBG (also called Vector-Bond Graph) is a vectorial extension of the regular Bond Graph. In systems where dynamical variables are related, their behavior can be represented with this concise form. Multi-bonds (see Fig. 18.b) are drawn as two parallel lines with power directions whereas regular Bonds (Fig. 18.a) use only one line.

The cardinality of the Multi-Bond is the number of single bonds grouped and is indicated inside the multi-bond. Here:

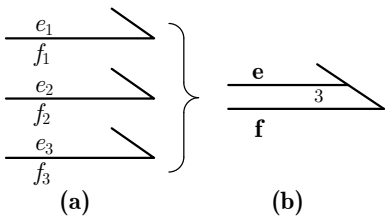

Fig. 18. Composition of a Multi-Bond.

$$\mathbf{e} = [e_1\ e_2\ e_3]^T \quad ; \quad \mathbf{f} = [f_1\ f_2\ f_3]^T \tag{21}$$

Notation used for elements remains unchanged but their parameters and/or modulating signals change from scalar to vector or matrix.

For sources (or modulated sources) the parameter (or variable) change from scalar to nx1 vector. See Fig. 19.

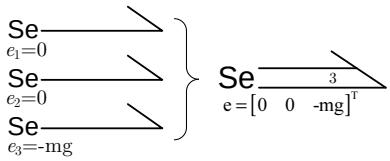

Fig. 19. Source of effort in Multi-Bond Graph.

For I-Elements and C-Elements, the intermediate vector variables **p** and **q** (momentum and displacement, respectively) are needed. For the linear case these variables are defined as

$$\mathbf{p} = \int \mathbf{e}\ dt = [p_1\ p_2\ \ldots\ p_n]^T \quad ; \quad p_i = \int e_i\ dt \tag{22}$$

$$\mathbf{q} = \int \mathbf{f}\ dt = [q_1\ q_2\ \ldots\ q_n]^T \quad ; \quad q_i = \int f_i\ dt \tag{23}$$

Using (22) for the I-Element and (23) for the C-Element, the constitutive relations of the 1-port elements are

$$\begin{aligned} \mathbf{p} = \mathbf{I}\ \mathbf{f} &\implies \text{I - Element} \\ \mathbf{q} = \mathbf{C}\ \mathbf{e} &\implies \text{C - Element} \\ \mathbf{e} = \mathbf{R}\ \mathbf{f} &\implies \text{R - Element} \end{aligned}$$

where I, C and R are the inertia, capacitance and resistance nxn matrices, respectively.

The extension of 1-junctions and 0-junctions to multi-bond graphs is straightforward and follows the same rules as those in scalar bond graphs:

$$\left.\begin{aligned} &\mathbf{f}_1 = \mathbf{f}_2 = \ldots = \mathbf{f}_n \\ &\mathbf{e}_1 + \mathbf{e}_2 + \ldots + \mathbf{e}_n \end{aligned}\right\} \text{1-Multi-junction}$$

$$\left.\begin{aligned} &\mathbf{e}_1 = \mathbf{e}_2 = \ldots = \mathbf{e}_n \\ &\mathbf{f}_1 + \mathbf{f}_2 + \ldots + \mathbf{f}_n \end{aligned}\right\} \text{0-Multi-junction}$$

Two port elements (gyrators and transformers) relate input/output multi-bonds in different manners. The general form of the transformation relationship (**A**) is a non-square matrix.

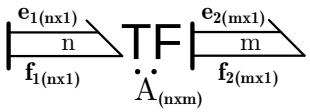

Fig. 20. Representation of a transformer in Multi-Bond Graph.

For the particular case of Fig. 20, the constitutive equations are:

$$\mathbf{e}_{1(\mathrm{nx1})} = \mathbf{A}_{(\mathrm{nxm})}\ \mathbf{e}_{2(\mathrm{mx1})}$$
$$\mathbf{f}_{2(\mathrm{mx1})} = \mathbf{A}^{T}_{(\mathrm{mxn})}\ \mathbf{f}_{1(\mathrm{nx1})}$$

The constitutive equations of the gyrator are obtained straightforward as

$$\mathbf{e}_{1(\mathrm{nx1})} = \mathbf{A}_{(\mathrm{nxm})}\ \mathbf{f}_{2(\mathrm{mx1})}$$
$$\mathbf{e}_{2(\mathrm{mx1})} = \mathbf{A}^{T}_{(\mathrm{mxn})}\ \mathbf{f}_{1(\mathrm{nx1})}$$

When both multi-bonds have the same cardinality (n=m) it is possible to make another useful transformation. Here **A** is a nx1 vector and the transformation is given by the following cross product

$$\mathbf{e}_{1(\mathrm{nx1})} = \mathbf{A}_{(\mathrm{nx1})} \times \mathbf{e}_{2(\mathrm{nx1})}$$
$$\mathbf{f}_{2(\mathrm{nx1})} = \mathbf{f}_{1(\mathrm{nx1})} \times \mathbf{A}_{(\mathrm{nx1})}$$

This transformation results useful in the following example.

A. Example

Elements in Fig. 21 are ideal undeformable rods considered massless. They are called "fixed translations" and they are commonly used to conform mechanical structures such as a vehicle chassis Fig. 21.a or robotic arms Fig. 21.b. The linkage between two "fixed translation" can be rigid (see Fig. 21.a) or can be made via a joint that gives certain degrees of freedom (revolute joint in Fig. 21.b).

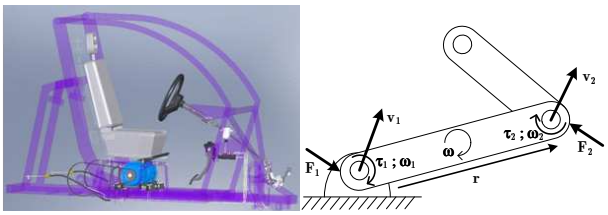

Fig. 21. Mechanical structures. a) Vehicle chassis b) Robotic arm.

Forces and velocities are given in the global frame whereas torques and angular velocities in the local frame. The set of equations derived from the free body diagram in Fig. 21.b is given by

$$\mathbf{v}_2 = \mathbf{v}_1 + \mathbf{R}\,(\boldsymbol{\omega} \times \mathbf{r}) \tag{24}$$
$$\mathbf{F}_2 = \mathbf{F}_1 \tag{25}$$
$$\boldsymbol{\omega}_1 = \boldsymbol{\omega}_2 \tag{26}$$
$$\boldsymbol{\tau}_1 = \boldsymbol{\tau}_2 + \mathbf{r} \times \mathbf{R}^T\ \mathbf{F} \tag{27}$$

Where **R** is the orthonormal orientation matrix that indicates the instantaneous orientation of the rod. It is used to transform vectors expressed in the local frame onto the global frame. The corresponding MBG representation is presented in Fig. 22.

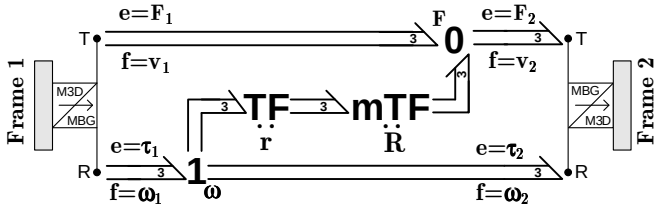

Fig. 22. Fixed Traslation MBG model.

Here (24) and (25) are graphically expressed in the "0" of the upper part whereas (26) and (27) are in the "1" of the lower part. The transformation relationships of the middle transformers are R and r that represents the length and orientation of the rod in the local frame.

The interfaces included on both extremes are used in the Dymola modelling environment to wrap the MBG model and then connect the elements via their frames.

REFERENCES

[1] Chan C. C.,"The State of the Art of Electric and Hybrid Vehicles", *Proceeding of IEEE*, Vol.90, Nº2, pp.247-275, 2002.

[2] A. M. Bos, "Modeling Multibody Systems in terms of Multibond Graphs, with application to a motorcycle", PhD thesis, Twente Univ. 1986.

[3] J. Jang, C. Han,"Proposition of a Modeling Method for Constrained Mechanical Systems Based on the Vector Bond Graph",*Journal of the Franklin Institute*, Vol. 335B, No 3, pp.451-469, 1998.

[4] F. Cellier, "Hierachical non-linear bond graph: A unified methodology for modelling complex physical systems" *Simulation*, Vol. 58, No 4, pp. 230-248, 1992.

[5] M. Dempsey, "Dymola for Multi-Engineering Modelling and Simulation",*Vehicle Power and Propulsion Conf. VPPC '06 IEEE*, pp 1-6, Sep. 2006.

[6] D. Zimmer,"A Modelica Library for MultiBond Graphs and its Application in 3D-Mechanics", *Master Thesis*, ETH Zürich, 2006.

[7] L. I. Silva, G. A. Magallán, C. H. De Angelo, and G. O. Garcia, "Vehicle Dynamics Using Multi-Bond Graphs: Four Wheel Electric Vehicle Modeling" *in 34th Ann. Conf. IEEE Ind. Electron. Soc. (IECON '08)*, pp. 2846-2851, Orlando, Florida, USA, Nov. 2008.

[8] H. B. Pacejka and R. S. Sharp,"Shear Force Developments by Pneumatic Tires in Steady State Conditions: A Review of modeling Aspects",*Vehicle Systems Dynamics 20*,pp. 121-176, 1991.

[9] P. C. Krause, O. Wasynczuk and S. Sudhoff *Analysis of Electric Machinery*, IEEE Press, New York, USA, 1994.

[10] D. Karnopp, "Understanding induction motor state equations using bond graph", *International Conference on Bond Graph Modeling and Simulation, ICBGM 2003*, Orlando, Florida, 2003.

[11] S. Junco, "Real and complex power bond graph modeling of the induction motor", *International Conf. on Bond Graph Modeling and Simulation, ICBGM 1999*, San Francisco, California, pp. 323-328, 1999.

[12] Krishnan R., *Electric Motor Drives: Modeling, Analysis and Control*, Prentice Hall, USA, 2001.

[13] G. Filippini, N. Nigro and S. Junco, "Vehicle dynamics simulation using bond graphs", *Proc. 3rd Int. Conf. IMAACA'2007*, February 2007.

[14] G. A. Magallán, C. H. De Angelo, G. Bisheimer, and G. O. Garcia, "A Neighborhood Electric Vehicle with Electronic Differential Traction Control" *in 34th Ann. Conf. IEEE Ind. Electron. Soc. (IECON '08)*, pp. 2757-2763, Orlando, Florida, USA, Nov. 2008.

[15] S. Behzadipour, A. Khajepour, "Causality in vector bond graphs and its application to modeling of multi-body dynamic systems" *Simulation Modelling Practice and Theory*, pp. 279-295, 2006.